

Quantitative ^{23}Na Magnetic Resonance Imaging in the Abdomen at 3 T

Jonathan R. Birchall¹, Ines Horvat-Menih,¹ Joshua D. Kaggie¹, Frank Riemer², Arnold J. V. Benjamin¹, Martin J. Graves¹, Ian Wilkinson³, *Ferdia A. Gallagher¹ and *Mary A. McLean¹

¹ Department of Radiology, University of Cambridge, Cambridge, United Kingdom

² Mohn Medical Imaging and Visualization Centre, Department of Radiology, Haukeland University Hospital Helse Bergen, Bergen, Norway

³ Cambridge Cardiovascular, University of Cambridge, Cambridge, United Kingdom

* These authors contributed equally to this work

Corresponding Author: Jonathan Birchall (jb2455@cam.ac.uk)

ABSTRACT

Object: To assess the feasibility of sodium-23 MRI for performing quantitative and non-invasive measurements of total sodium concentration (TSC) and relaxation in a variety of abdominal organs.

Materials and Methods: Proton and sodium imaging of the abdomen was performed in 19 healthy volunteers using a 3D cones sequence and a sodium-tuned 4-rung transmit/receive body coil on a clinical 3 T system. The effects of B_1 non-uniformity on TSC measurements were corrected using the double-angle method. The long-component of ^{23}Na T_2^* relaxation time was measured using a series of variable echo-times.

Results: The mean and standard deviation of TSC and long-component ^{23}Na T_2^* values were calculated across the healthy volunteer group in the kidneys, cerebrospinal fluid (CSF), liver, gallbladder, spleen, aorta, and inferior vena cava.

Discussion: Mean TSC values in the kidneys, liver, and spleen were similar to those reported using ^{23}Na -MRI previously in the literature. Measurements in the CSF and gallbladder were lower, potentially due to the reduced spatial resolution achievable in a clinically acceptable scan time. Mean long-component ^{23}Na T_2^* values were consistent with previous reports from the kidneys and CSF. Intra-population standard error was larger in smaller, fluid-filled structures due to fluid motion and partial volume effects.

Keywords – sodium MRI; quantification, tissue sodium content, relaxation, abdomen

INTRODUCTION

Magnetic Resonance Imaging (MRI) is a powerful tool for routine and exploratory clinical diagnostic imaging of the human body without the need for ionising radiation or invasive biopsies. Whilst routine proton MRI techniques are widely applicable in the imaging of both tissue structure and function owing to the abundance of protons in body fat and water, imaging of other biologically-relevant and MR-active X-nuclei such as sodium-23 is also possible. Existing techniques for quantification of sodium content such as flame photometry,[1,2] ion-specific electrochemical potentiometric techniques,[3,4] or inductively-coupled plasma optical emission spectroscopy (ICP-OES)[5] are well-documented in the intracellular and extracellular compartments,[6,7] but all require tissue acquisition which is invasive. Non-invasive techniques such as urinary osmolarity have been used to study the corticomedullary gradient (CMG) in the kidneys, but these provide only indirect and non-specific

information on kidney function, and are not widely translatable to other organs.[8]

In addition to hydrolysis of ATP and the phosphorylation of the Na^+/K^+ pump, endogenous sodium exchange between the intracellular and the extracellular compartments plays an essential role in numerous biological pathways including regulation of blood volume, pressure and pH, as well as neuronal activation and maintenance of the cell resting potential.[9] However, excessive dietary sodium intake has been linked to numerous health risks, with increased blood pressure in particular being a contributing factor in the prevalence of heart disease, chronic kidney disease and stroke among others.[10-12] Previous histological studies have shown the total sodium concentration (TSC) to be elevated by more than 50% in malignant brain and breast tumours in humans in comparison with healthy tissue, and changes in sodium content are thought to correlate with successful treatment.[13,14] Additionally, there is

a clinical need for the differentiation of tumour types and cellular sodium uptake and retention may provide an opportunity to discriminate more aggressive from less aggressive tumours.

Quantitative analysis of the combined sodium content from both the intracellular and extracellular compartments using MRI has been demonstrated in a number of prior studies,[9,15-18] and further progress in the field is arising from advancements in dedicated ^{23}Na -tuned radiofrequency (RF) coil design, pulse sequence development and data analysis.[18-28] There is therefore an interest in establishing ^{23}Na -MRI as a quantitative imaging biomarker for cellular integrity and metabolism in disease diagnosis. Recent human imaging studies have included the determination of tumour cellularity in ovarian cancer,[29] quantification of sodium in prostate tumours,[30] linking of elevated skin sodium content to multiple sclerosis[31] and psoriasis,[32] as well as the measurement of tissue sodium accumulation in chronic kidney disease (CKD).[33,34] *Ex vivo* ^{23}Na MR spectroscopy of human tissue has also been utilised to observe a reduction in skin sodium content in Type 2 diabetes,[35] and determination of the salt-sensitivity of blood pressure (SSBP) using ^{23}Na MRI may be potentially useful as a non-invasive, quantitative imaging biomarker for hypertension.[36,37]

Additionally, measurements of the transverse relaxation time (T_2^*) could potentially provide information on tissue oxygenation; measuring the inverse relaxation rate ($R_2^* = 1/T_2^*$) in proton MR has shown elevation in the presence of paramagnetic deoxyhaemoglobin.[38] Quantitative proton T_2^* mapping has been demonstrated as a potential biomarker in the imaging of tumour hypoxia[39,40] and in the prognostic staging of rectal cancer[41]. Quantification of ^{23}Na T_2^* in humans has proven challenging due to additional relaxation effects arising from the quadrupolar nature of the ^{23}Na nucleus ($I = 3/2$), where spin relaxation follows a bi-exponential trend with one decay component being substantially longer than the other.[49, 50] Multiple quantum filtering techniques for separating these decay components have been demonstrated in the human brain, but have yet to find wider application due to the order of magnitude lower signal intensity relative to the single quantum spin-density-weighted imaging.[51, 52] Additionally, the larger and less-efficient coils employed in abdominal imaging necessitate longer pulse widths to achieve desired flip angles, by which

point the short T_2^* relaxation component has already decayed to a significant extent, limiting the achievable SNR. To this end, *in vivo* evaluation of T_2^* estimation in other organs and fluid-filled structures for the first time is of interest to complement previous work in the healthy human kidneys.[42,43]

In this study, we report estimates of total ^{23}Na content (TSC) and long-component transverse relaxation (T_2^*) in eight organs and fluid-filled structures within the abdomen of healthy volunteers (N = 19, 12M/7F).

MATERIALS AND METHODS

This study was approved by the local ethical review committee (reference number 08-H0311-117).

1. Data Acquisition

Axial ^{23}Na MR images of the abdomen were acquired using a novel birdcage transmit/receive body coil, possessing a large (~ 48 cm) field-of-view (FOV) which facilitated uniform excitation over a significant portion of the abdomen in subjects with a range of body habitus, as we have previously described[44]. Corresponding axial proton images were acquired at 3 T using a clinical GE MR750 system (GE Healthcare, Waukesha WI). A pair of 50 mL Falcon tubes, each containing an 80 mM agar gel sodium chloride phantom, were suspended from the upper rungs on either side of the ^{23}Na birdcage coil (Figure 1) to serve as a calibration standard for signal intensity. In later subjects, two further identical phantoms were placed underneath the patient to the left and right sides of the bed centre, to serve as an additional point of reference.

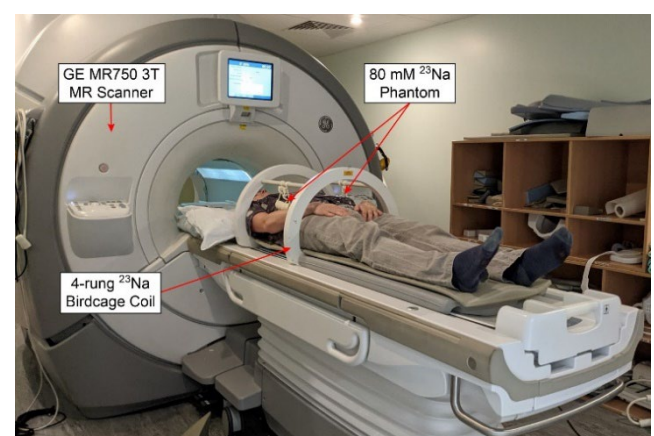


Fig. 1 Orientation of healthy volunteers, the ^{23}Na birdcage T/R body coil and 80 mM agar gel phantoms within the 3 T body MRI scanner

Healthy volunteers were situated headfirst and supine inside the ^{23}Na birdcage coil, with the centre of the coil positioned over the kidneys, as confirmed using a fast

gradient echo (FGRE) ^1H localiser sequence. Anatomical fat/water ^1H imaging was achieved using an axial breath-hold 3D T_1 -weighted sequence (LAVA-Flex GRE) with the MR system body coil and 32 locations each (TEs = 1.1/2.2 ms, TR = 3.7 ms, flip = 15° , averages = 1, matrix = 256x192, phase FOV = 0.7, FOV = 40 cm). Shims were optimized over a large (~16 cm diameter) cuboid region and these shim settings were retained in the following multinuclear scans.

A multinuclear Bloch-Siegert based calibration scan sequence[45] was prescribed in the centre of the coil to determine the centre frequency of ^{23}Na and suitable transmit and receive gain values; all values were kept constant for the duration of the scanning session to ensure consistent intensity scaling. A pair of low-resolution images were acquired using a 3D cones trajectory (FOV = 48 cm, TR = 150 ms, TE = 0.705 ms, flip angle = $40/80^\circ$, trajectory resolution = $9 \times 9 \times 9$ mm, 197 transients, averages = 3, 125 kHz full receiver bandwidth, total duration = 1:28 mins per sequence) to perform B_1 non-uniformity correction using the Double-Angle Method (DAM).[46-48]

A higher-resolution 3D conical trajectory (FOV = 48 cm, TR = 100 ms, TE = 0.705 ms, flip angle = 70° , voxel size = $4 \times 4 \times 8$ mm, 1402 transients, averages = 5, 167 kHz full receiver bandwidth, total duration = 11:41 mins) was used to acquire maps of ^{23}Na signal intensity across the abdomen.[49] Lastly, a series of six low-resolution series were acquired with a further 3D cones trajectory (FOV = 48 cm, TR = 100 ms, flip angle = 70° , trajectory resolution = $9 \times 9 \times 9$ mm, 197 transients, averages = 4, 125 kHz full receiver bandwidth, total duration = 1:19 mins per series) were performed at a range of echo times (TEs = 0.705, 1.5, 2, 4, 8 and 16 ms) in order to generate quantitative maps of the ^{23}Na T_2^* relaxation time constant across the abdomen. Low-resolution images spatially matched the location and FOV of the high-resolution counterpart in each subject.

2. MATLAB Data Analysis

All data analysis and region drawing were performed in MATLAB (Mathworks, Natick MA).

2.1. B_1 Field Inhomogeneity Correction

For each subject, a map of the relative B_1 value at each voxel was generated from the corresponding intensity ratio of high (80°)-to-low (40°) flip-angle intensity in the two low-resolution DAM series datasets as:

$$relB1(x, y, z) = \cos^{-1} \left(\frac{I(x, y, z)_{high}}{2 \cdot I(x, y, z)_{low}} \right) / \alpha_{low} \quad (1)$$

where I_{high} and I_{low} are the signal intensities at each voxel in the high and low flip-angle datasets respectively, and α_{low} is the lower of the two flip-angles used (nominally 40° in our protocol). A 3D median filter (kernel size = $5 \times 5 \times 5$ voxels) was applied to maximise the signal-to-noise ratio (SNR) whilst preserving edge information. Example output from the 3D median filtering process in MATLAB is presented in Figure S1 of the Supporting Information (SI). Thresholding was performed so that the signal intensity ratio was made equal to zero for voxels in the high flip-angle dataset, possessing an intensity less than 10% of the maximum observed value. Lastly, values were normalised to generate a value of 1000 when the actual and nominal flip angles were equal.

It should be noted that for some of the healthy volunteers, B_1 mapping data was not acquired as part of the imaging protocol. To perform B_1 non-uniformity correction in these subjects, a population average estimate B_1 map was created by taking the median non-zero B_1 value at every voxel across all the remaining subjects ($N = 17$) and using this as a reference when determining the effective total sodium concentration.

Three-dimensional maps of the B_1 -corrected total tissue sodium concentration (TSC) were calculated from the high-resolution 3D cones trajectory series in each of the $N = 19$ healthy volunteers as 80 mM multiplied by the ratio of the pixel intensity to the average intensity in a region of interest (ROI) drawn inside the calibration phantom. A coronal maximum intensity projection (MIP), shown in Figure S2 of the Supporting Information was additionally acquired in one subject, but was not used for the purposes of TSC estimation.

However, due to non-linear image distortions which differed between the DAM and high-resolution ^{23}Na series (shown in Figure S3 of the Supporting Information and discussed in more detail in SI Section 2), a single image transform could not be applied to adequately register both volumes to the ^1H anatomical series. Additionally, the tissue contrast of the DAM series was insufficient to reliably register specific regions and structures to the corresponding ^1H anatomical image. Generation of B_1 -corrected TSC maps across the whole abdomen was therefore considered unreliable. To this end, TSC calculation was

instead performed by undertaking B_1 non-uniformity correction on a per-region basis, drawing a region for each organ or fluid-filled structure in both the high-resolution ^{23}Na image and the low-resolution DAM B_1 map. Region TSC was then calculated by accounting for the receive and transmit B_1 profiles as follows:

$$C_{organ} = C_{ref} \cdot \frac{I_{organ}}{I_{ref}} \cdot \frac{B1_{ref}}{B1_{organ}} \cdot \frac{\sin(\alpha \cdot B1_{ref})}{\sin(\alpha \cdot B1_{organ})} \quad (2)$$

where I_{organ} and I_{ref} represent the image intensities in the drawn organ and phantom regions in the high-resolution ^{23}Na image, whilst $B1_{ref}$ and $B1_{organ}$ represent the corresponding normalised intensities in the drawn regions of the B_1 map. C_{ref} is the total sodium concentration of the agar gel phantom used as a reference (80 mM in our study). In this way, the uncorrected TSC is derived from the first two terms of Equation (2), the receive B_1 correction is applied in the third term, and the transmit B_1 correction applied in the final term. The nominal flip angle α in the high-resolution dataset was 70° .

Estimates of TSC from all regions of interest presented in this work have been presented as concentrations in mmol per litre of wet tissue. Absolute quantification of TSC (which would include relaxation corrections) was not performed, although relaxation bias for longitudinal T_1 relaxation and the long component of T_2^* relaxation was assumed to be small based on the repetition time and echo time of RF pulses used in signal acquisition ($TR = 100 \text{ ms} \gg T_1$ and $TE = 0.705 \text{ ms} \ll T_{2^*_{long}}$). More information on relaxation bias estimation can be found in Tables S1 and S2 in Section 3 of the Supporting Information (SI).

2.2. ^{23}Na T_2^* Relaxation Time Constant Calculation

Three-dimensional maps of the T_2^* relaxation time constant were calculated from the low-resolution 3D cones trajectory variable TE series in each of the healthy volunteers by taking the negative natural logarithm of the signal intensity at echo times from 2 to 16 ms and performing a linear fit (the first two echo times were not used for analysis, see Figure S4 in the Supporting Information). Thresholding was again performed relative to 10% of the maximum observed signal intensity in the shortest echo time series ($TE = 0.705 \text{ ms}$), with intensities below this value set to zero.

For the purposes of this work, estimates of the long T_2^* components only were determined for each organ or structure via log-linear fitting. A comparison of mono-exponential, bi-exponential and log-linear estimation

of T_2^* in this body of work is included in Section 3 of the Supporting Information (SI).

2.3. Region Drawing

Regions of interest were drawn on a single axial slice within MATLAB using the *roipoly* function to create logical masks over the structure or organ in both datasets, with the mean intensity values in these drawn regions only being used in the TSC and long-component ^{23}Na T_2^* calculations. Slice selection was performed manually for each organ and volunteer by visually identifying a slice with minimal artifacts and/or partial volume effects from other nearby structures and void spaces. Regions drawn were as follows: phantoms, kidneys, CSF, liver, gallbladder, spleen, aorta, and inferior vena cava (IVC)

As discussed above, the TSC calculation required the drawing of regions within both the high-resolution and low-resolution, DAM datasets to perform B_1 non-uniformity correction. For the long-component T_2^* calculation, regions drawn mirrored those used in the B_1 calculations. Regions were drawn in the image series acquired using the highest flip angle for DAM and the shortest TE for T_2^* to maximise SNR. Regions were drawn of the approximate size, shape, and location as those shown in Figure 2. Additionally, a single large region was drawn outside of the body habitus to perform signal-to-noise ratio (SNR) measurements of uncorrected high-resolution ^{23}Na signal intensity.

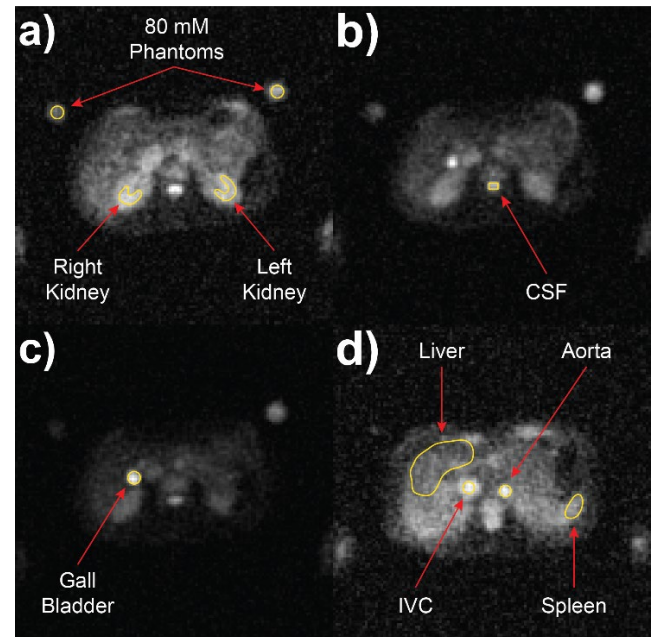


Fig. 2 a) Example images acquired from high-resolution 3D conical trajectory axial slices in a female healthy volunteer (age 25-30 years), illustrating the region-drawing process in MATLAB: a) both kidneys and both phantoms; b) CSF; c)

gallbladder; d) spleen, liver, aorta, and inferior vena cava (IVC)

RESULTS

A total of nineteen healthy volunteers (12 male, 7 female) underwent imaging for the purposes of this study.

1. Double-Angle Method (DAM) B_1 Mapping

Example low-flip and high-flip ^{23}Na images are presented in Figures 3a and 3b, respectively, along with a corresponding ^1H anatomical image of summed water and fat shown in Figure 3c. The resulting B_1 map

created from these low-resolution ^{23}Na images is shown in Figure 3d, with the population average estimate B_1 map utilised for subjects without DAM acquisition series shown in Figure 3f). Lastly, a high-resolution ^{23}Na TSC map was generated before applying B_1 correction, as presented in Figure 3e. All images shown were acquired from a central axial slice. The population average estimate B_1 map shown in Figure 3f includes data from all volunteers where DAM B_1 data were acquired; all other images were acquired in a single healthy male volunteer (age 25-30 years).

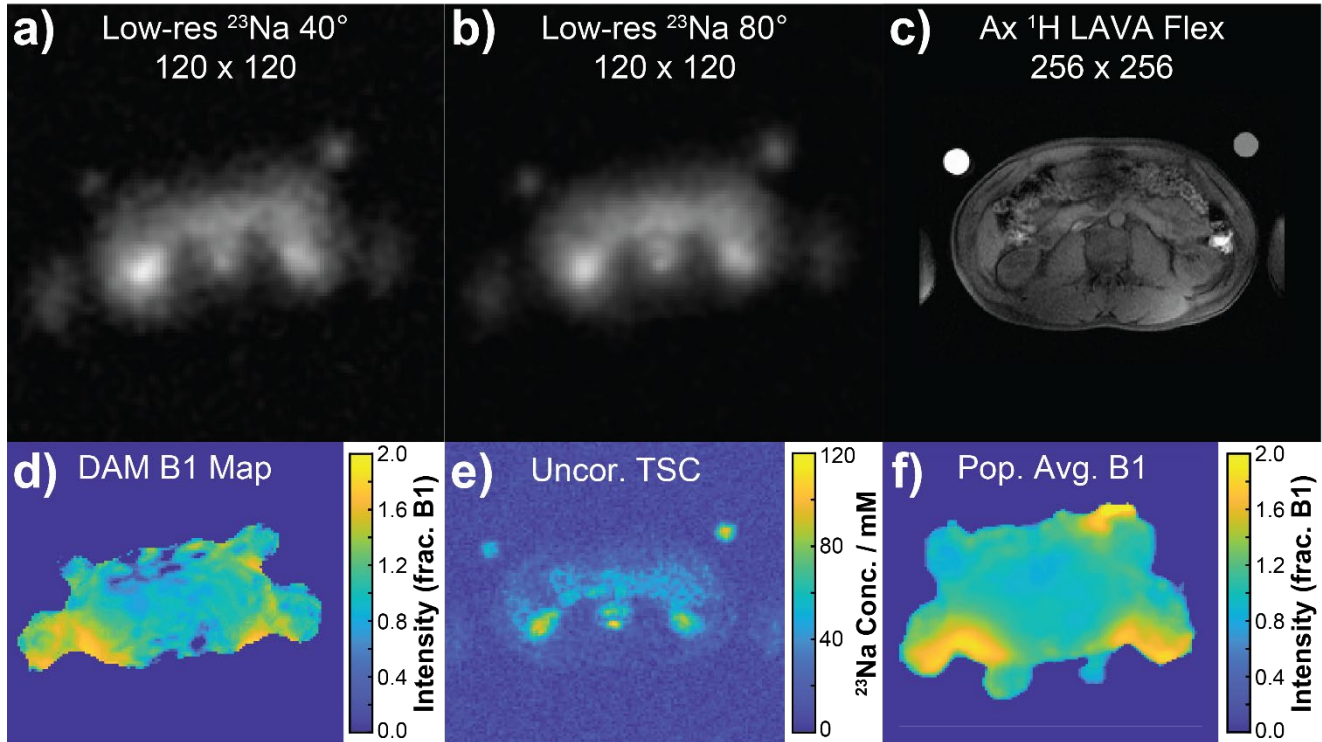


Fig. 3 Example sodium images. a) low-resolution ^{23}Na signal intensity image at a 40° flip angle; b) low-resolution ^{23}Na signal intensity image at an 80° flip angle; c) fused fat/water anatomical ^1H image (acquisition FOV = 40 cm, scaled to match other displays); d) relative B_1 intensity map calculated using the double-angle method; e) high-resolution uncorrected ^{23}Na signal intensity map; f) population average estimate B_1 intensity map. All images were acquired from an axial slice through the centre of the abdomen. Data presented in display f) represents the median B_1 across all volunteers where DAM B_1 data were acquired; all other displays present data from a single healthy male volunteer (age 25-30 years) exclusively. Circles visible in the upper-left and upper-right sides of the FOV correspond to the suspended 80 mM agar NaCl phantoms

Mean SNR of uncorrected ^{23}Na signal intensity per-region across the healthy volunteer population was highest in the gall bladder (33 ± 15), followed by the CSF (30 ± 4) and kidneys (left: 23 ± 5 , right: 26 ± 5). SNR was comparable in the aorta (21 ± 3) and IVC (22 ± 4). The lowest SNR values from uncorrected ^{23}Na signal intensity images were seen in the spleen (13 ± 3) and liver (11 ± 3). SNR values for individual subjects by region can be found in Table S3 of the Supporting Information.

2. Total Sodium Concentration

Intensity maps of acquired ^{23}Na signal through a healthy male volunteer (age 30-35 years) are shown in Figure 4. As discussed previously, the mean total sodium content in each organ was not determined directly from the TSC map due to non-linear image distortion between the high-resolution and DAM B_1 ^{23}Na series. B_1 -corrected ^{23}Na TSC values were calculated independently for each organ or structure in all subjects, and are recorded in Table S3 of the Supporting Information (SI). Median ^{23}Na TSC values

and their associated interquartile ranges are presented in Figure 5. For all values quoted below, the uncertainty is expressed as the population standard deviation.

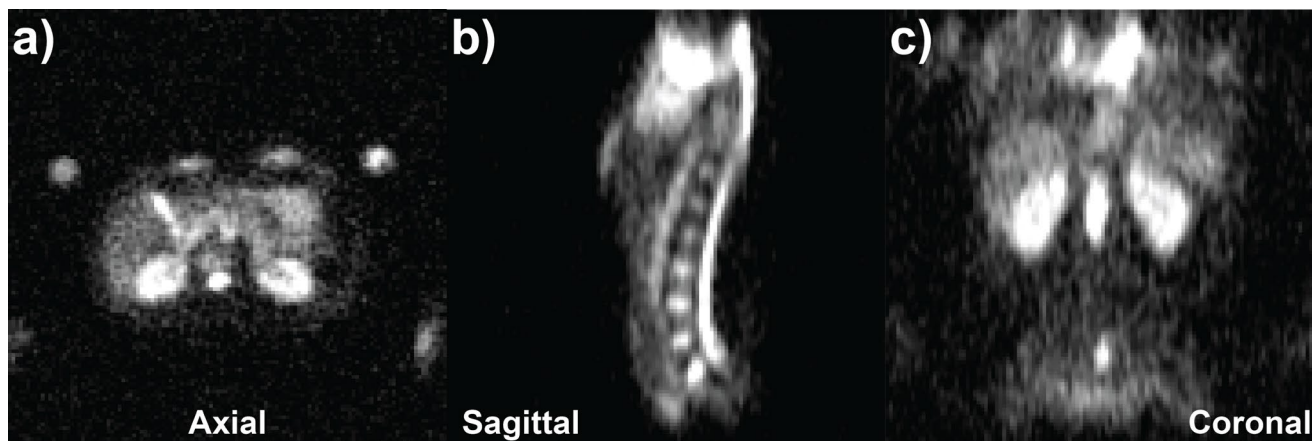


Fig. 4 ^{23}Na signal intensity maps in axial, sagittal and coronal planes demonstrating sodium content in some major organs and fluid-filled regions of interest in a healthy male volunteer (age 30-35 years)

Across the 19 healthy volunteers, the ^{23}Na TSC was highest in the gallbladder with a mean value of 122 ± 42 mM, followed by the CSF, where the estimated mean TSC was calculated to be 94 ± 18 mM. High standard deviation of TSC was also observed in other small, fluid-filled structures such as the aorta and IVC, where mean TSC values were 78 ± 16 mM and 83 ± 21 mM, respectively. In the kidneys, the coefficient of variation in measured total sodium concentration were somewhat reduced: 79 ± 15 mM and 71 ± 9 mM TSC in the left and right kidneys, respectively. The liver and spleen demonstrated a low sodium content and correspondingly high coefficients of variations, with observed TSC values of 41 ± 10 mM in the liver and 40 ± 9 mM, respectively.

3. ^{23}Na T_2^* Relaxation Time Constant

An example ^{23}Na long T_2^* quantitative map across a single central slice centred on the kidneys from a healthy female volunteer (age 35-40 years) is presented in Figure 6c, alongside the corresponding

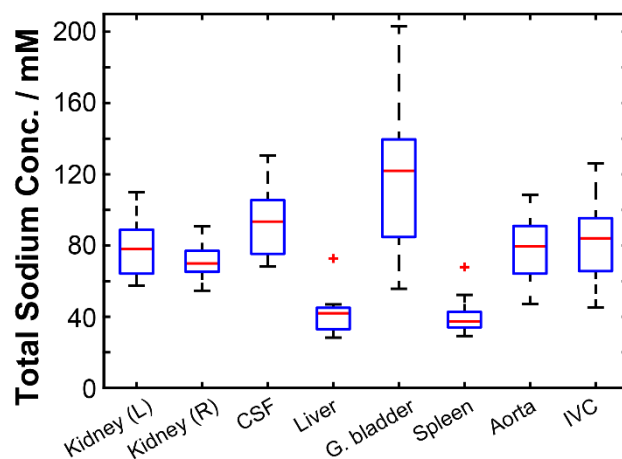


Fig. 5 Total ^{23}Na concentration box-and-whisker plots illustrating the median (red line), interquartile range (blue box) and maximum extent of non-outlier data points (dashed black lines) for each of the regions of interest interrogated. Whiskers were defined as having a maximum extent of 1.5 times the IQR for each ROI. Note that the values reported for small structures are likely underestimated relative to true concentrations reported in the literature due to partial volume effects

shortest-TE image in Figure 6b for comparison. Median long-component ^{23}Na T_2^* values and their associated interquartile ranges are presented in Figure 7. Numerical ^{23}Na T_2^* values calculated for each organ and structure in all healthy volunteers are displayed in Table S4 of the Supporting Information (SI).

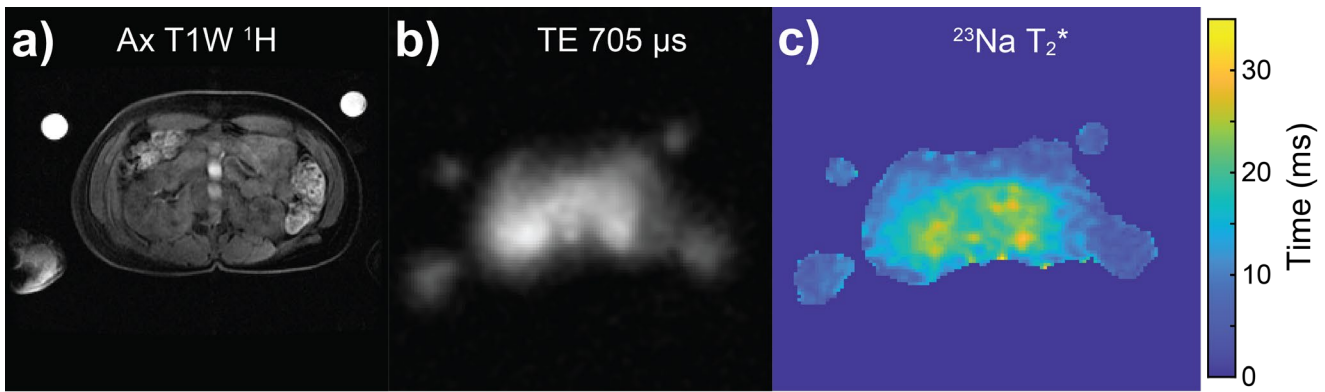


Fig. 6 a) Anatomical ^1H T_1 -weighted image through a central axial slice centred on the kidneys for a healthy female volunteer (age 35-40 years). A corresponding axial low-resolution ^{23}Na image from the series with the shortest TE (0.705 ms, not used for long-component T_2^* estimation) is shown in display b), whilst a single axial slice map of long-component ^{23}Na T_2^* is shown in display c)

Mean long-component T_2^* values were highest in the kidneys: 23 ± 3 ms in both cases. Relaxation was observed to be significantly more rapid in the liver with a moderate coefficient of variation (11 ± 3 ms). Whilst exhibiting a higher average long-component T_2^* value than the liver, intra-population variation was similarly modest in the blood: 17 ± 4 ms in the aorta and 16 ± 4 ms in the IVC. Long-component T_2^* relaxation time was observed to be highest in the CSF at 25 ± 5 ms. As with the B_1 -corrected TSC calculations, the most significant intra-population variation in the long-component T_2^* value was typically observed in the gallbladder (16 ± 6 ms), as well as the spleen (10 ± 4 ms).

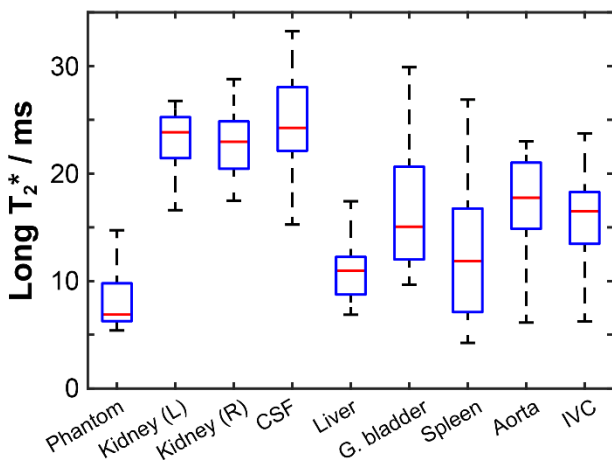


Fig. 7 ^{23}Na long-component T_2^* relaxation time constant box-and-whisker plots illustrating the median (red line), interquartile range (blue box) and maximum extent of non-outlier data points (dashed black lines) for each of the regions of interest interrogated. Whiskers were defined as having a maximum extent of 1.5 times the IQR for each ROI

DISCUSSION

1. Double-Angle Method (DAM) B_1 Mapping

The uncorrected ^{23}Na TSC map through a central axial slice shown in display 3f shows the sharp spatial resolution of the two agar gel phantoms, both kidneys and the CSF and spinal cord, facilitating easy region drawing within MATLAB and quantification of mean ^{23}Na signal on a per-region basis, as discussed in the following section.

The B_1 maps presented in Figures 3d and 3f demonstrate that most organs investigated in this study are within a central region of the abdomen where B_1 variation in this coil was relatively small: mean fractional B_1 value = 0.97 ± 0.07 in the population average B_1 map. The most significant B_1 variation was localised to structures near the rungs of the birdcage T/R body coil, with maximum fractional intensities as high as double those seen in the central region. Three-plane maps of median fractional B_1 and accompanying standard deviation across the $N = 17$ healthy volunteers where DAM B_1 maps were acquired can be found in Figure S5 of the Supporting Information (SI).

In addition to the large variation in B_1 intensity near the coil rungs which made the correction estimates less reliable, the displacement of the agar gel phantoms used for TSC calibration towards the edge of the FOV could significantly impact TSC calculation due to the prevalence of image distortions inherent in the cones sequence at the FOV edge. Whilst not observed in the healthy volunteer population, to avoid any potential future bias when imaging large participants, this observation led to the inclusion of two additional identical phantoms beneath the patient support, displaced either side of the bed centre. These additional, fixed phantoms could be used as a point of reference in the event of the suspended phantoms yielding poor SNR.

2. Total Sodium Concentration

Estimated TSC values in the gall bladder (122 ± 42 mM) and CSF (94 ± 18 mM) were lower than established reports in the literature of ~ 145 mM sodium concentration in bile[50] and 151 mM in CSF in humans[51] as measured via ion chromatography and those observed in a previous quantification via ^{23}Na -MRI[52]. This discrepancy, as well as high standard deviation of TSC values amongst the healthy volunteer population, was theorised to arise from partial volume effects due to the small region size, since this prior study was conducted using sagittal and coronal plane imaging which presents a significantly larger potential region of interest for CSF than in the axial plane used in this work. Use of a higher spatial resolution would reduce the effects of partial volume errors, but this naturally increases scan time and may impact clinical tolerability.

In contrast, values in the blood vessels were in reasonable agreement with those expected based on a normal extracellular sodium concentration range for healthy adults of 135-145 mM as measured in blood serum,[53] coupled with a typical haematocrit fraction or red blood cell volume of ~ 40 -45% in the total blood volume.[54] The difference in sodium content within the aorta and IVC was not statistically significant at a 5% level of significance (aorta = 78 ± 16 mM, IVC = 83 ± 21 mM, $p = 0.052$).

TSC values within the kidneys (left = 79 ± 15 mM, right = 71 ± 9 mM) were around 20 mM lower than those estimated in previous *in vivo* ^{23}Na -MRI assessment of the medulla[43] and whole-kidney TSC,[55] but were approximately 20 mM higher than those estimated elsewhere using a FLORET B_1 non-uniformity correction method.[56] The difference in TSC values observed between the left and right kidneys across our healthy control group was found to be statistically significant at a 5% level of significance ($p = 0.029$). This unexpected result likely arises from small imperfections in the B_1 correction applied using our low spatial resolution DAM image series. The variation in B_1 is more pronounced near to the kidneys due to proximity of the coil rungs, as visible in Figure 3f.

The relatively similar standard deviation values for the liver and spleen indicates that they may be primarily driven by the noise floor. The total sodium concentration values in the liver (41 ± 10 mM) were in agreement with previously-reported studies in healthy rats,[57-59] but substantially greater than those

observed previously in human studies undertaken using surface coils.[60] Flame photometric studies in Dahl rats similarly identified low splenic sodium content relative to other organs[57] (40 ± 9 mM in this work).

3. ^{23}Na T_2^* Relaxation Time Constant

^{23}Na T_2^* values from the different abdominal regions generally fell within the range of previously-reported long ^{23}Na T_2^* values.[9,61]

The low observed intra-population standard deviation of long-component T_2^* in the kidneys was expected for large organs with high relative ^{23}Na signal intensity, owing to reduced variability resulting from partial volume effects. Measurements of ^{23}Na T_2^* in the kidneys were in agreement with previous reports of 21 ± 1 ms at 3 T[43] and 7 T.[42,62] Unlike the renal TSC values, the difference in T_2^* relaxation times observed between the left and right kidneys was not affected by B_1 variation, and was not statistically significant at a 5% level of significance (left kidney = 23.2 ± 2.5 ms, right kidney = 22.7 ± 3.1 ms, $p = 0.644$).

The relatively short T_2^* values observed in the liver (10.7 ± 2.7 ms) are in agreement with previous ^1H -MRI studies which identified a significantly increased component of short- T_2^* tissue in the liver relative to long- T_2^* counterparts,[63-65] but are lower than those reported in rat liver.[66] This observation is thought to arise predominantly from the high content of paramagnetic iron within the liver, which has the effect of increasing ^{23}Na relaxation rates.[67,68]

Observations of ^{23}Na T_2^* in the blood were contrary to the expectations that both the rate of relaxation and the intra-population variation would be higher due to partial volume effects and the influence of fluid flow given the spatial resolution used for acquisition.[69-71] Oxygenated (aorta) and deoxygenated (IVC) blood relaxation rates *in vivo* were observed to be statistically different at a 5% level of significance (aorta = 17.3 ± 4.2 ms, IVC = 15.7 ± 4.0 ms, $p = 0.013$). This observation was expected considering the different magnetic properties of oxyhaemoglobin (diamagnetic) and deoxyhaemoglobin (weakly paramagnetic), as demonstrated by the higher signal intensity of oxygenated blood in T_2^* -weighted BOLD fMRI.[72,73]

Fluid motion effects on T_2^* relaxation in the CSF were not considered to be significant due to the slower rate of CSF motion relative to blood[74] and compared to the spatial imaging resolution employed here.

However, the low spatial resolution may explain why the calculated values (24.6 ± 4.6 ms in this work) were significantly below those reported in studies of the brain at 7 T.[75]

^{23}Na T_2^* estimates in the gall bladder were limited by the small region size, whereas quantification in the spleen suffered from an inherently low relative ^{23}Na signal intensity. Observation of the shortest long-component T_2^* values in the spleen is consistent with reports in a murine model comparing relaxation properties with that of the heart and liver,[76]

although in that study, a statistically significant difference between spleen and liver relaxation rates was noted, which is not observed here (gall bladder = 15.8 ± 6.0 ms, spleen = 10.3 ± 4.2 ms, $p = 0.188$). Human studies of ^1H transverse relaxation rates also highlighted faster relaxation in the liver than in the spleen[77] which has not been observed for ^{23}Na .

A comparison of results observed in this work with those published elsewhere in the literature is summarised in Table 1 for reference.

Table 1: Comparison of calculated TSC and T_2^* relaxation values to previously published work.

TOTAL SODIUM CONCENTRATION / mM				
Region	Study	Population	Value(s) Reported	Notes
Kidneys	Grist 2020[55]	12 (11M/1F)	94±5, 91±6	Two-site repeatability study, whole kidney measurement
	Haneder 2013[43]	50 (30M/20F)	99±18	Medulla measurement only
	Vaeggemose 2023[56]	5 (3M/2F)	53±27	FLORET B_1 correction
CSF	Çavuşoğlu 2022[52]	5 (2M/3F)	148±7	
Liver	Hooper 1976[58]	18 (9M/9F)	37±3	Quantification in rats using flame photometry
	Tsunooka 1997[57]	8 (all M)	33±1	Quantification in rats using flame photometry
	James 2015[60]	3 (2M/1F)	20±1	2x surface coil array, B_1 correction via large homogeneous phantom
Gall bladder	Furey 1966[50]	208 (76M/132F)	145	Measured in patients undergoing surgery
Spleen	Tsunooka 1997[57]	8 (all M)	25±1	Quantification in rats using flame photometry
T_2^* RELAXATION TIME / ms				
Region	Study	Population	Value(s) Reported	Notes
Kidneys	Haneder 2014[42]	8 (4M/4F)	21±1	Medulla value, obtained at 7 T
	Haneder 2013[43]	6 (2M/4F)	21±1	Mono-exponential fitting
CSF	Nagel 2011[75]	3 (unspecified)	56±4	Mono-exponential fitting w/ 7 T head birdcage coil, $5.5 \times 5.5 \times 5.5$ mm ³

CONCLUSIONS

We have demonstrated the potential for acquisition of ^{23}Na signal intensity across a large proportion of the abdomen using ^{23}Na -MRI and a large-FOV sodium-tuned T/R body coil with good signal-to-noise ratio in a clinically acceptable timespan. Subsequent estimation of DAM B_1 -corrected total sodium concentration and the long-component of the transverse ^{23}Na T_2^* relaxation time in a variety of abdominal organs and fluid-filled structures has been demonstrated. This

work will serve as a baseline to evaluate pathological changes in conditions such as hypertension and for tumour characterisation. It is hoped that the development of ^{23}Na -MRI as a biomarker for tissue sodium content and dynamics may in the future inform clinical management by reducing the need for invasive biopsy techniques.

Two identical 80 mM agar gel sodium chloride phantoms were used to estimate TSC in this work to serve as a reliability test, since differences in phantom

location can result in variation in local B_1 , and may also experience variation in RF artifacts. Additionally, phantoms may dry out over time, increasing their effective sodium concentration. An alternative method for estimation of ^{23}Na TSC which has been demonstrated in studies in the leg[78] and intervertebral discs[52] and could be applied to future work makes use of multiple agar gel phantoms of different concentrations and performing a linear fit through the ^{23}Na signal intensities of each phantom and the organ or structure of interest. Presumably, as in these studies, the phantom arrangement should also occupy a fixed position within the coil, such as underneath the patient, to make phantom B_1 calibration measurements more consistent, and phantoms could also be larger in size to facilitate easier region drawing. This may be particularly important in larger patients, as the suspended-phantom arrangement utilised in this work may be less reliable when phantoms are displaced close to the rungs of the coil or the edge of the field-of-view, but at the same time should not impede patient comfort. Estimation of ^{23}Na T_2^* measurements in fluid-filled regions might be made more reliable using cardiac-triggered acquisition to suppress the effects of fluid motion, but this would have the consequence of significantly increasing scan durations.

Analysis of anatomical variation in TSC and correlations with other MR-based metrics could be facilitated by automated registration of anatomical ^1H , low-resolution DAM B_1 and uncorrected high-resolution TSC images. This may be made easier with the use of machine-learning or deep-learning registration techniques, to overcome the difficulties presented by image rotations and distortions prevalent with conical trajectories possessing long readout lengths.

ACKNOWLEDGEMENTS

This research was supported by the NIHR Cambridge Biomedical Research Centre (BRC-1215-20014); the views expressed are those of the authors and not necessarily those of the NIHR or the Department of Health and Social Care. The authors acknowledge funding support from the National Cancer Imaging Translational Accelerator (NCITA), Cancer Research UK, the Cambridge Experimental Cancer Medicine Centre,

the Cancer Research UK Cambridge Centre, the Mark Foundation Institute for Integrated Cancer Medicine (MFICM) and the Canadian Institute For Advanced Research.

SUPPORTING INFORMATION

Additional methodological descriptions of B_1 median filtering, sodium cones non-linear image distortions and T_2^* relaxation time estimation via log-linear and exponential fitting. Full tabulated measurements of B_1 -corrected total sodium concentration and long-component ^{23}Na T_2^* in each region and healthy volunteer are provided. Data analysis scripts used in MATLAB are not included but will be shared upon request.

DECLARATIONS

1. Funding or Competing Interests

The authors have no relevant financial or non-financial interests to disclose.

2. Ethical Approval

All imaging of human participants was performed in accordance with the ethical standards of the 1964 Helsinki Declaration and its later amendments and comparable ethical standards. The study was approved by the local ethical review committee (reference number 08-H0311-117).

3. Informed Consent

Informed consent was obtained from all individual subjects prior to their participation in the study.

4. Author Contributions

JRB: Study conception and design, Acquisition of data, Analysis and interpretation of data, Drafting of Manuscript. IHM: Study conception and design, Critical revision. JDK: Study conception and design, Critical Revision. FR: Study conception and design, Critical revision. AJVB: Study conception and design, Acquisition of data. MJG: Critical revision. IW: Study conception and design. FAG: Study conception and design, Critical Revision. MAM: Study conception and design, Acquisition of data, Analysis and interpretation of data, Drafting of Manuscript, Critical revision.

REFERENCES

1. Overman RR, Davis AK (1947) The application of flame photometry to sodium and potassium determinations in biological fluids. *J Biol Chem* 168 (2):641-649.
2. MacDonald NF, Williams PZ, Burton JI, Batsakis JG (1981) Sodium and potassium measurements: direct potentiometry and flame photometry. *Am J Clin Pathol* 76 (4 Suppl):575-577.
3. Kricka LJ, Park JY (2014) Assay Principles in Clinical Pathology. In: McManus LM, Mitchell RN (eds) *Pathobiology of Human Disease*. Academic Press, San Diego, pp 3207-3221.
4. Castle-Kirsbaum M, Kyi M, Wright C, Goldschlager T, Danks RA, Parkin WG (2021) Hyponatraemia and hypernatraemia: Disorders of Water Balance in Neurosurgery. *Neurosurgical Review* 44 (5):2433-2458.
5. Dipietro ES, Bashor MM, Stroud PE, Smarr BJ, Burgess BJ, Turner WE, Neese JW (1988) Comparison of an inductively coupled plasma-atomic emission spectrometry method for the determination of calcium, magnesium, sodium, potassium, copper and zinc with atomic absorption spectroscopy and flame photometry methods. *Sci Total Environ* 74:249-262.
6. Tashiro M, Tursun P, Konishi M (2005) Intracellular and extracellular concentrations of Na⁺ modulate Mg²⁺ transport in rat ventricular myocytes. *Biophys J* 89 (5):3235-3247.
7. Lo CJ, Leake MC, Berry RM (2006) Fluorescence measurement of intracellular sodium concentration in single *Escherichia coli* cells. *Biophys J* 90 (1):357-365.
8. Akbari A, Lemoine S, Salerno F, Marcus TL, Duffy T, Scholl TJ, Filler G, House AA, McIntyre CW (2022) Functional Sodium MRI Helps to Measure Corticomedullary Sodium Content in Normal and Diseased Human Kidneys. *Radiology* 303 (2):384-389.
9. Ouwerkerk R (2011) Sodium MRI. In: Modo M, Bulte JWM (eds) *Magnetic Resonance Neuroimaging: Methods and Protocols*. Humana Press, Totowa, NJ, pp 175-201.
10. Strazzullo P, D'Elia L, Kandala N-B, Cappuccio FP (2009) Salt intake, stroke, and cardiovascular disease: meta-analysis of prospective studies. *BMJ* 339:b4567.
11. Whelton PK, Appel LJ, Sacco RL, Anderson CAM, Antman EM, Campbell N, Dunbar SB, Frohlich ED, Hall JE, Jessup M, Labarthe DR, MacGregor GA, Sacks FM, Stamler J, Vafiadis DK, Horn LVV (2012) Sodium, Blood Pressure, and Cardiovascular Disease. *Circulation* 126 (24):2880-2889.
12. Nerbass FB, Pecoits-Filho R, McIntyre NJ, McIntyre CW, Taal MW (2015) High sodium intake is associated with important risk factors in a large cohort of chronic kidney disease patients. *European Journal of Clinical Nutrition* 69 (7):786-790.
13. Ouwerkerk R, Bleich KB, Gillen JS, Pomper MG, Bottomley PA (2003) Tissue Sodium Concentration in Human Brain Tumors as Measured with ²³Na MR Imaging. *Radiology* 227 (2):529-537.
14. Ouwerkerk R, Jacobs MA, Macura KJ, Wolff AC, Stearns V, Mezban SD, Khouri NF, Bluemke DA, Bottomley PA (2007) Elevated tissue sodium concentration in malignant breast lesions detected with non-invasive ²³Na MRI. *Breast Cancer Res Treat* 106 (2):151-160.
15. Madelin G, Regatte RR (2013) Biomedical applications of sodium MRI in vivo. *J Magn Reson Imaging* 38 (3):511-529.
16. Hu R, Kleimaier D, Malzacher M, Hoesl MAU, Paschke NK, Schad LR (2020) X-nuclei imaging: Current state, technical challenges, and future directions. *Journal of Magnetic Resonance Imaging* 51 (2):355-376.
17. Zaric O, Juras V, Szomolanyi P, Schreiner M, Raudner M, Giraud C, Trattning S (2021) Frontiers of Sodium MRI Revisited: From Cartilage to Brain Imaging. *Journal of Magnetic Resonance Imaging* 54 (1):58-75.
18. Gast LV, Platt T, Nagel AM, Gerhalter T (2023) Recent technical developments and clinical research - applications of sodium (²³Na) MRI. *Progress in Nuclear Magnetic Resonance Spectroscopy* 138-139:1-51.
19. Steidle G, Graf H, Schick F (2004) Sodium 3-D MRI of the human torso using a volume coil. *Magnetic Resonance Imaging* 22 (2):171-180.
20. Wetterling F, Corteville DM, Kalayciyan R, Rennings A, Konstandin S, Nagel AM, Stark H, Schad LR (2012) Whole body sodium MRI at 3T using an asymmetric birdcage resonator and short echo time sequence: first images of a male volunteer. *Phys Med Biol* 57 (14):4555-4567.
21. Bangerter NK, Kaggie JD, Taylor MD, Hadley JR (2016) Sodium MRI radiofrequency coils for body imaging. *NMR Biomed* 29 (2):107-118.
22. Malzacher M, Kalayciyan R, Konstandin S, Haneder S, Schad LR (2016) Sodium-23 MRI of whole spine at 3 Tesla using a 5-channel receive-only phased-array and a whole-body transmit resonator. *Z Med Phys* 26 (1):95-100.
23. Platt T, Umatham R, Fiedler TM, Nagel AM, Bitz AK, Maier F, Bachert P, Ladd ME, Wielpütz MO, Kauczor HU, Behl NGR (2018) In vivo self-gated (²³Na) MRI at 7 T using an oval-shaped body resonator. *Magn Reson Med* 80 (3):1005-1019.
24. Anisimov NV, Sadykhov EG, Pavlova OS, Fomina DV, Tarasova AA, Pirogov YA (2019) Whole Body Sodium MRI at 0.5 Tesla Using Surface Coil and Long

- Echo Time Sequence. *Applied Magnetic Resonance* 50 (10):1149-1161.
25. Boehmert L, Kuehne A, Waiczies H, Wenz D, Eigentler TW, Funk S, von Knobelsdorff-Brenkenhoff F, Schulz-Menger J, Nagel AM, Seeliger E, Niendorf T (2019) Cardioresnal sodium MRI at 7.0 Tesla using a 4/4 channel $^1\text{H}/^{23}\text{Na}$ radiofrequency antenna array. *Magnetic Resonance in Medicine* 82 (6):2343-2356.
26. Malzacher M, Chacon-Caldera J, Paschke N, Schad LR (2019) Feasibility study of a double resonant ($^1\text{H}/^{23}\text{Na}$) abdominal RF setup at 3T. *Zeitschrift für Medizinische Physik* 29 (4):359-367.
27. Milani B, Delacoste J, Burnier M, Pruijm M (2019) Exploring a new method for quantitative sodium MRI in the human upper leg with a surface coil and symmetrically arranged reference phantoms. *Quant Imaging Med Surg* 9 (6):985-999.
28. Wilferth T, Mennecke A, Gast LV, Lachner S, Müller M, Rothhammer V, Huhn K, Uder M, Doerfler A, Nagel AM, Schmidt M (2022) Quantitative 7T sodium magnetic resonance imaging of the human brain using a 32-channel phased-array head coil: Application to patients with secondary progressive multiple sclerosis. *NMR Biomed* 35 (12):e4806.
29. Deen SS, Riemer F, McLean MA, Gill AB, Kaggie JD, Grist JT, Crawford R, Latimer J, Baldwin P, Earl HM, Parkinson CA, Smith SA, Hodgkin C, Moore E, Jimenez-Linan M, Brodie CR, Addley HC, Freeman SJ, Moyle PL, Sala E, Graves MJ, Brenton JD, Gallagher FA (2019) Sodium MRI with 3D-cones as a measure of tumour cellularity in high grade serous ovarian cancer. *European Journal of Radiology Open* 6:156-162.
30. Barrett T, Riemer F, McLean MA, Kaggie J, Robb F, Tropp JS, Warren A, Bratt O, Shah N, Gnanapragasam VJ, Gilbert FJ, Graves MJ, Gallagher FA (2018) Quantification of Total and Intracellular Sodium Concentration in Primary Prostate Cancer and Adjacent Normal Prostate Tissue With Magnetic Resonance Imaging. *Invest Radiol* 53 (8):450-456.
31. Huhn K, Linz P, Pemsel F, Michalke B, Seyferth S, Kopp C, Chaudri MA, Rothhammer V, Dörfler A, Uder M, Nagel AM, Müller DN, Waschbisch A, Lee D-H, Bäuerle T, Linker RA, Haase S (2021) Skin sodium is increased in male patients with multiple sclerosis and related animal models. *Proceedings of the National Academy of Sciences* 118 (28):e2102549118.
32. Maifeld A, Wild J, Karlsen TV, Rakova N, Wistorf E, Linz P, Jung R, Birukov A, Gimenez-Rivera V-A, Wilck N, Bartolomaeus T, Dechend R, Kleinewietfeld M, Forslund SK, Krause A, Kokolakis G, Philipp S, Clausen BE, Brand A, Waisman A, Kurschus FC, Wegner J, Schultheis M, Luft FC, Boschmann M, Kelm M, Wiig H, Kuehne T, Müller DN, Karbach S, Markó L (2022) Skin Sodium Accumulates in Psoriasis and Reflects Disease Severity. *Journal of Investigative Dermatology* 142 (1):166-178.
33. Qirjazi E, Salerno FR, Akbari A, Hur L, Penny J, Scholl T, McIntyre CW (2020) Tissue sodium concentrations in chronic kidney disease and dialysis patients by lower leg sodium- 23 magnetic resonance imaging. *Nephrology Dialysis Transplantation* 36 (7):1234-1243.
34. Salerno FR, Akbari A, Lemoine S, Scholl TJ, McIntyre CW, Filler G (2023) Effects of pediatric chronic kidney disease and its etiology on tissue sodium concentration: a pilot study. *Pediatr Nephrol* 38 (2):499-507.
35. Hanson P, Philp CJ, Randeve HS, James S, O'Hare JP, Meersmann T, Pavlovskaya GE, Barber TM (2021) Sodium in the dermis colocalizes to glycosaminoglycan scaffold, with diminishment in type 2 diabetes mellitus. *JCI Insight* 6 (12):e145470.
36. Kopp C, Linz P, Dahlmann A, Hammon M, Jantsch J, Müller DN, Schmieder RE, Cavallaro A, Eckardt K-U, Uder M, Luft FC, Titze J (2013) ^{23}Na Magnetic Resonance Imaging-Determined Tissue Sodium in Healthy Subjects and Hypertensive Patients. *Hypertension* 61 (3):635-640.
37. Martin K, Tan S-J, Toussaint ND (2022) Magnetic resonance imaging determination of tissue sodium in patients with chronic kidney disease. *Nephrology* 27 (2):117-125.
38. Panek R, Welsh L, Dunlop A, Wong KH, Riddell AM, Koh DM, Schmidt MA, Doran S, McQuaid D, Hopkinson G, Richardson C, Nutting CM, Bhide SA, Harrington KJ, Robinson SP, Newbold KL, Leach MO (2016) Repeatability and sensitivity of T2^* measurements in patients with head and neck squamous cell carcinoma at 3T. *J Magn Reson Imaging* 44 (1):72-80.
39. O'Connor JPB, Robinson SP, Waterton JC (2019) Imaging tumour hypoxia with oxygen-enhanced MRI and BOLD MRI. *The British Journal of Radiology* 92 (1096):1-12 (20180642).
40. Robinson SP, Howe FA, Rodrigues LM, Stubbs M, Griffiths JR (1998) Magnetic resonance imaging techniques for monitoring changes in tumor oxygenation and blood flow. *Seminars in Radiation Oncology* 8 (3):197-207.
41. Peng Y, Luo Y, Hu X, Shen Y, Hu D, Li Z, Kamel I (2021) Quantitative T2^* -Weighted Imaging and Reduced Field-of-View Diffusion-Weighted Imaging of Rectal Cancer: Correlation of R2^* and Apparent Diffusion Coefficient With Histopathological Prognostic Factors. *Front Oncol* 11:670156.
42. Haneder S, Juras V, Michaely HJ, Deligianni X, Bieri O, Schoenberg SO, Trattng S, Zbýň Š (2014) In vivo sodium (^{23}Na) imaging of the human kidneys at 7 T:

- Preliminary results. *European Radiology* 24 (2):494-501.
43. Haneder S, Kettner P, Konstandin S, Morelli JN, Schad LR, Schoenberg SO, Michaely HJ (2013) Quantitative in vivo ^{23}Na MR imaging of the healthy human kidney: determination of physiological ranges at 3.0T with comparison to DWI and BOLD. *Magnetic Resonance Materials in Physics, Biology and Medicine* 26 (6):501-509.
44. Kaggie JD, Lanz T, McLean MA, Riemer F, Schulte RF, Benjamin AJV, Kessler DA, Sun C, Gilbert FJ, Graves MJ, Gallagher FA (2021) Combined (23) Na and (13) C imaging at 3.0 Tesla using a single-tuned large FOV birdcage coil. *Magn Reson Med* 86 (3):1734-1745.
45. Sacolick LI, Wiesinger F, Hancu I, Vogel MW (2010) B1 mapping by Bloch-Siegert shift. *Magn Reson Med* 63 (5):1315-1322.
46. Cunningham CH, Pauly JM, Nayak KS (2006) Saturated double-angle method for rapid B1+ mapping. *Magn Reson Med* 55 (6):1326-1333.
47. Allen SP, Morrell GR, Peterson B, Park D, Gold GE, Kaggie JD, Bangerter NK (2011) Phase-sensitive sodium B1 mapping. *Magn Reson Med* 65 (4):1125-1130.
48. Lommen J, Konstandin S, Krämer P, Schad LR (2016) Enhancing the quantification of tissue sodium content by MRI: time-efficient sodium B1 mapping at clinical field strengths. *NMR Biomed* 29 (2):129-136.
49. Gurney PT, Hargreaves BA, Nishimura DG (2006) Design and analysis of a practical 3D cones trajectory. *Magnetic Resonance in Medicine* 55 (3):575-582.
50. Furey AT (1966) Hyponatremia after choledochostomy and T tube drainage. *The American Journal of Surgery* 112 (6):850-855.
51. Harrington MG, Salomon RM, Pogoda JM, Oborina E, Okey N, Johnson B, Schmidt D, Fonteh AN, Dalleska NF (2010) Cerebrospinal fluid sodium rhythms. *Cerebrospinal Fluid Research* 7:3.
52. Çavuşoğlu M, Pazahr S, Ciritsis AP, Rossi C (2022) Quantitative ^{23}Na -MRI of the intervertebral disk at 3 T. *NMR in Biomedicine* 35 (8):e4733.
53. Dmitrieva NI, Liu D, Wu CO, Boehm M (2022) Middle age serum sodium levels in the upper part of normal range and risk of heart failure *European Heart Journal* 43 (35):3335-3348.
54. Billett HH (1990) Hemoglobin and Hematocrit. In: Walker HK, Hall WD, Hurst JW (eds) *Clinical Methods: The History, Physical, and Laboratory Examinations*. Boston.
55. Grist JT, Riemer F, Hansen ESS, Tougaard RS, McLean MA, Kaggie J, Bøgh N, Graves MJ, Gallagher FA, Laustsen C (2020) Visualization of sodium dynamics in the kidney by magnetic resonance imaging in a multi-site study. *Kidney International* 98 (5):1174-1178.
56. Vaeggemose M, Schulte RF, Laustsen C (2023) Clinically feasible B1 field correction for multi-organ sodium imaging at 3 T. *NMR in Biomedicine* 36 (2):e4835.
57. Tsunooka K, Morita H (1997) Effect of a chronic high-salt diet on whole-body and organ sodium contents of Dahl rats. *Journal of Hypertension* 15 (8):851-856.
58. Hooper G, Dick DA (1976) Nonuniform distribution of sodium in the rat hepatocyte. *Journal of General Physiology* 67 (4):469-474.
59. Everett JL, Day CL, Bergel F (1964) Analysis of August rat liver for calcium, copper, iron, magnesium, manganese, molybdenum, potassium, sodium and zinc*. *Journal of Pharmacy and Pharmacology* 16 (2):85-90.
60. James JR, Panda A, Lin C, Dydak U, Dale BM, Bansal N (2015) In vivo sodium MR imaging of the abdomen at 3T. *Abdom Imaging* 40 (7):2272-2280.
61. Riemer F, Solanky BS, Wheeler-Kingshott CAM, Golay X (2018) Bi-exponential ^{23}Na T2* component analysis in the human brain. *NMR in Biomedicine* 31 (5):e3899.
62. Zbyn S, Juras V, Michaely HJ, Deligianni X, Bieri O, Schoenberg SO, Trattnig S, Haneder S (2013) Sodium T2* Mapping of the Human Kidneys in Vivo at 7 Tesla. *Proc Intl Soc Mag Reson Med* 21:4142.
63. Bernardino ME, Small W, Goldstein J, Sewell CW, Sones PJ, Gedgudas-McClees K, Galambos JT, Wenger J, Casarella WJ (1983) Multiple NMR T2 relaxation values in human liver tissue. *AJR Am J Roentgenol* 141 (6):1203-1208.
64. Westwood MA, Anderson LJ, Firmin DN, Gatehouse PD, Lorenz CH, Wonke B, Pennell DJ (2003) Interscanner reproducibility of cardiovascular magnetic resonance T2* measurements of tissue iron in thalassemia. *J Magn Reson Imaging* 18 (5):616-620.
65. Zhu A, Hernando D, Johnson KM, Reeder SB (2019) Characterizing a short T(2) * signal component in the liver using ultrashort TE chemical shift-encoded MRI at 1.5T and 3.0T. *Magn Reson Med* 82 (6):2032-2045.
66. Bansal N, Germann MJ, Seshan V, Shires GT, 3rd, Malloy CR, Sherry AD (1993) Thulium 1,4,7,10-tetraazacyclododecane-1,4,7,10-tetrakis(methylene phosphonate) as a ^{23}Na shift reagent for the in vivo rat liver. *Biochemistry* 32 (21):5638-5643.
67. Wood JC, Enriquez C, Ghugre N, Tyzka JM, Carson S, Nelson MD, Coates TD (2005) MRI R2 and R2* mapping accurately estimates hepatic iron concentration in transfusion-dependent thalassemia and sickle cell disease patients. *Blood* 106 (4):1460-1465.
68. Hernando D, Levin YS, Sirlin CB, Reeder SB (2014) Quantification of liver iron with MRI: state of the art

- and remaining challenges. *J Magn Reson Imaging* 40 (5):1003-1021.
69. Wexler L, Bergel DH, Gabe IT, Makin GS, Mills CJ (1968) Velocity of Blood Flow in Normal Human Venae Cavae. *Circulation Research* 23 (3):349-359.
70. Stein PD, Sabbah HN, Anbe DT, Walburn FJ (1979) Blood velocity in the abdominal aorta and common iliac artery of man. *Biorheology* 16:249-255.
71. Vieli A, Moser U, Maier S, Meier D, Boesiger P (1989) Velocity profiles in the normal human abdominal aorta: A comparison between ultrasound and magnetic resonance data. *Ultrasound in Medicine & Biology* 15 (2):113-119.
72. Ogawa S, Lee TM, Kay AR, Tank DW (1990) Brain magnetic resonance imaging with contrast dependent on blood oxygenation. *Proc Natl Acad Sci U S A* 87 (24):9868–9872.
73. Whang JS, Kolber M, Powell DK, Libfeld E (2015) Diffusion-weighted signal patterns of intracranial haemorrhage. *Clinical Radiology* 70 (8):906-916.
74. Battal B, Kocaoglu M, Bulakbasi N, Husmen G, Sanal HT, Tayfun C (2011) Cerebrospinal fluid flow imaging by using phase-contrast MR technique. *The British Journal of Radiology* 84 (1004):758-765.
75. Nagel AM, Bock M, Hartmann C, Gerigk L, Neumann J-O, Weber M-A, Bendszus M, Radbruch A, Wick W, Schlemmer H-P, Semmler W, Biller A (2011) The Potential of Relaxation-Weighted Sodium Magnetic Resonance Imaging as Demonstrated on Brain Tumors. *Investigative Radiology* 46 (9):539-547.
76. Jackson LH, Vlachodimitropoulou E, Shangaris P, Roberts TA, Ryan TM, Campbell-Washburn AE, David AL, Porter JB, Lythgoe MF, Stuckey DJ (2017) Non-invasive MRI biomarkers for the early assessment of iron overload in a humanized mouse model of β -thalassemia. *Scientific Reports* 7 (1):43439.
77. Schwenzer NF, Machann J, Haap MM, Martirosian P, Schraml C, Liebig G, Stefan N, Häring H-U, Claussen CD, Fritsche A, Schick F (2008) T2* Relaxometry in Liver, Pancreas, and Spleen in a Healthy Cohort of One Hundred Twenty-Nine Subjects—Correlation With Age, Gender, and Serum Ferritin. *Investigative Radiology* 43 (12):854-860.
78. Gast LV, Baier LM, Chaudry O, Meixner CR, Müller M, Engelke K, Uder M, Heiss R, Nagel AM (2023) Assessing muscle-specific potassium concentrations in human lower leg using potassium magnetic resonance imaging. *NMR Biomed* 36 (1):1-13 (e4819).